

# Role of excimer formation and induced photoemission on the Ar metastable kinetics in atmospheric pressure Ar-NH 3 dielectric barrier discharges

Raphaël Robert, Gerjan Hagelaar, Nader Sadeghi, Romain Magnan, Luc Stafford, Françoise Massines

▶ **To cite this version:**

Raphaël Robert, Gerjan Hagelaar, Nader Sadeghi, Romain Magnan, Luc Stafford, et al.. Role of excimer formation and induced photoemission on the Ar metastable kinetics in atmospheric pressure Ar-NH 3 dielectric barrier discharges. Plasma Sources Science and Technology, 2022, 31 (6), pp.065010. 10.1088/1361-6595/ac7748 . hal-03765065

**HAL Id: hal-03765065**
**https://cnrs.hal.science/hal-03765065**

Submitted on 30 Aug 2022

**HAL** is a multi-disciplinary open access archive for the deposit and dissemination of scientific research documents, whether they are published or not. The documents may come from teaching and research institutions in France or abroad, or from public or private research centers.

L'archive ouverte pluridisciplinaire **HAL**, est destinée au dépôt et à la diffusion de documents scientifiques de niveau recherche, publiés ou non, émanant des établissements d'enseignement et de recherche français ou étrangers, des laboratoires publics ou privés.

# Role of excimer formation and induced photoemission on the Ar metastable kinetics in atmospheric pressure Ar-$NH_3$ dielectric barrier discharges

**Raphaël Robert[1,2], Gerjan Hagelaar[3], Nader Sadeghi[4], Romain Magnan[1], Luc Stafford[2], Françoise Massines[1*]**

[1]Laboratoire Procédés Matériaux et Énergie Solaire (PROMES, CNRS, UPR 8521), Rambla de la thermodynamique, 66100 Perpignan, France

[2]Département de physique, Université de Montréal, 1375 ave Thérèse-Lavoie-Roux, Montréal, Québec, H2V 0B3, Canada

[3] Laboratoire Plasma et Conversion d'Énergie (LAPLACE, CNRS, UMR5213), 118 Route de Narbonne, 31077 Toulouse, France

[4]Laboratoire Interdisciplinaire de Physique (LIPhy CNRS, UMR 5588), Laboratoire des Technologies de la Microélectronique (LTM, CNRS, UMR 5129), Université de Grenoble-Alpes, Grenoble, France

[*] Electronic mail: francoise.massines@promes.cnrs.fr

# Abstract

Tunable diode laser absorption spectroscopy was used to record the space-and time-resolved number density of argon metastable atoms, Ar($1s_3$) (Paschen notation), in plane-to-plane dielectric barrier discharges operated in a Penning Ar-$NH_3$ mixture at atmospheric pressure. In both low-frequency (LF 650 V, 50 kHz) discharges and dual LF-radiofrequency (RF 190 V, 5 MHz) discharges operated in $\alpha$-$\gamma$ mode, the density of Ar($1s_3$) revealed a single peak per half-period of the LF voltage, with rise and decay times in the sub-microsecond time scale. These results were compared to the predictions of a 1D fluid model based on continuity and momentum equations for electrons, argon ions ($Ar^+$ and $Ar_2^+$) and excited argon 1s atoms as well electron energy balance equation. Using the scheme commonly reported for Ar-based dielectric barrier discharges in the homogeneous regime, the Ar metastable kinetics exhibited much slower rise and decay times than the ones seen in the experiments. The model was improved by considering the fast creation of $Ar_2$* excimers through 3-body reactions involving Ar(1s) atoms and the rapid loss of $Ar_2$* by vacuum ultraviolet light emission. In optically thin media for such photons, they can readily reach the dielectric barriers of the DBD electrodes and induce secondary electron emission. It is shown that $Ar_2$* and photoemission play a significant role not only on the Ar metastable kinetics, but also on the dominant ionization pathways and possible $\alpha$-$\gamma$ transition in dual frequency RF-LF discharges.



**Keywords**: Dielectric barrier discharges, Tunable laser diode absorption spectroscopy, Dual-frequency discharges, Fluid modeling, Argon excited dimer, Photoemission.

# 1. Introduction

The use of dielectric barrier discharges (DBDs) at atmospheric pressure has experienced uninterrupted growth since the 2000s. Their field of applications is widening, ranging from surface engineering [1–7], control flow [8,9], plasma catalyses [10], pollution control [11], or ozone production [12–14]. This diversification of applications is accompanied by the development of new DBD regimes [15]. In addition to the filamentary and patterned discharge regimes [16,17], homogenous discharges in Townsend, glow or RF $\alpha$ and $\gamma$ modes are also used [18–22], including for thin film deposition [3,15]. New excitation waveforms for homogenous discharges have also been proposed, including dual-frequency [23–26], frequency-shift keying [27,28] or sawtooth tailored discharges [29]. In low-frequency (LF) plasmas, metastable states play a major role in maintaining the discharge in a homogeneous regime [30]. As a result of their very small diffusion transport, they can remain in the DBD gap from one cycle of the applied voltage to the other. This so-called memory effect can contribuate to secondary electron emission at the walls and can induce a pre-ionization of the gas [31,32]. In a Penning gas mixture, for example He with $N_2$ or Ar with $NH_3$, metastable species can also induce excitation and ionization at low applied voltage via stepwise excitation and ionization [33–37]. For atmospheric-pressure plasmas sustained in noble gases such as Ar, many authors have reported significant vacuum ultraviolet (VUV) emission [38–43]. While VUV photons at 104.8 and 106.7 nm emanating from Ar 1s resonant states (Paschen notation) are usually trapped due to high populations of ground-state Ar atoms (optically thick medium) [44], the continuum emission linked to argon excimers at 126 nm is characterized by much longer absorption lengths (optically thin medium) [43,45]. Such photons can thus induce a number of additional surface and gas phase phenomena, including secondary electron emission [46]. However, the contribution of such mechanism was never explicitly explored for homogeneous DBDs.

In this work, tunable diode laser absorption spectroscopy (TDLAS) is used to record the population of metastable argon $1s_3$ atoms in plane-to-plane DBDs operated in a Penning Ar-$NH_3$ mixture at atmospheric pressure as a function of time at two locations in the inter-electrode gap for both LF and dual-frequency LF-RF excitations. Through a comparison of TDLAS measurements with the predictions of a 1D fluid model [25,47], it is found that VUV photons emitted by $Ar_2$* dimers, created by 3-body reactions involving Ar(1s) species and two ground state Ar atoms, can induce photoelectron emission at the dielectrics surface of the cathode and can thus play a very significant role on the physics driving Ar-based DBDs.

## 2. Experimental setup

The DBD examined in this study relies on two plane-to-plane 50 x 10 mm² metallic electrodes covered by 1 mm-thick 70 x 70 mm² dielectric plates made of alumina and separated by a 2mm gap. The discharge zone is thus fixed to a 50 x 10 x 2 $mm^3$ volume. The whole DBD cell is contained in an air-tighten chamber. Before each experiment, the chamber was pumped down to $10^{-5}$ bar and then flushed with Ar + 200 ppm of $NH_3$ at 3 standard liters per minute (SLM) flow rate. A needle valve between the chamber and the pumping pipe allows fixing the total pressure in the chamber to 1 bar. Considering the dimensions of the gap, the flow is laminar between dielectric plates. As shown in Figure 1, the top electrode is powered by a 50 kHz LF generator, while the bottom electrode is either grounded or powered by a 5 MHz RF generator. Note that, in a DBD, the applied voltage ($V_a$) is different from the voltage across the gap ($V_{gas}$ – called "gas voltage" in this paper) due to the voltage drop across both top ($V_{ds1}$) and bottom ($V_{ds2}$) dielectric plates ($V_a = V_{ds1} + V_{gas} + V_{ds2}$). This voltage drop is caused by charges present in the discharge, collected on the dielectric surfaces, inducing a modification of the gas voltage. Here, LF and RF waveforms are both produced by a single generator (Keysight 33500B Series), which synchronizes their phases. To produce dual-frequency discharges, the LF signal at 50 kHz is brought to the reactor through an audio amplifier (Crest CC4000) connected to a bridged resistance and a step-up voltage transformer (Boige & Vignal). As for the RF signal at 5 MHz, it is sent to a broadband power amplifier (Prana GN500) linked to a custom-made transformer. In this study, the amplitude of the LF and RF voltages are set to 650 V and 190 V, respectively. Current-voltage characteristics are recorded using a current probe and two high-voltage probes (Tektronix P6015A 75 MHz); all signals are visualized on an oscilloscope (Tektronix MSO56).

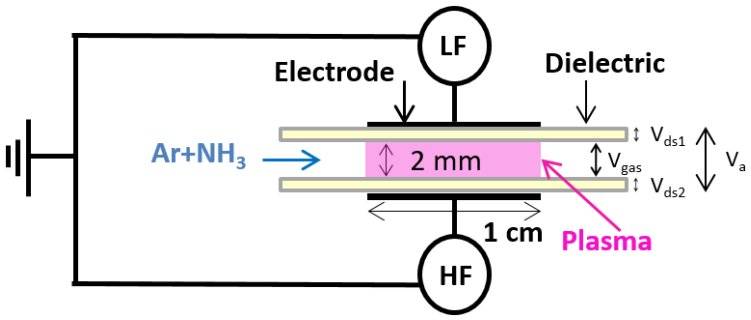



*Figure 1. Schematics of the plane-to-plane dielectric barrier discharge with dual-frequency excitation.*

# 3. Measurement of argon metastable atoms

As shown in Figure 2, a tunable diode laser working around 772 nm (DFB, DL100, Toptica) is used to record the number density of Ar metastable atoms by absorption spectroscopy [48–50]. In this wavelength range, atoms in the most populated Ar($1s_5$) metastable state can absorb the laser light on $1s_5$-$2p_7$ transition at 772.38 nm and atoms in the other metastable state Ar($1s_3$) can absorb the laser light on $1s_3$-$2p_2$ transition at 772.42 nm.

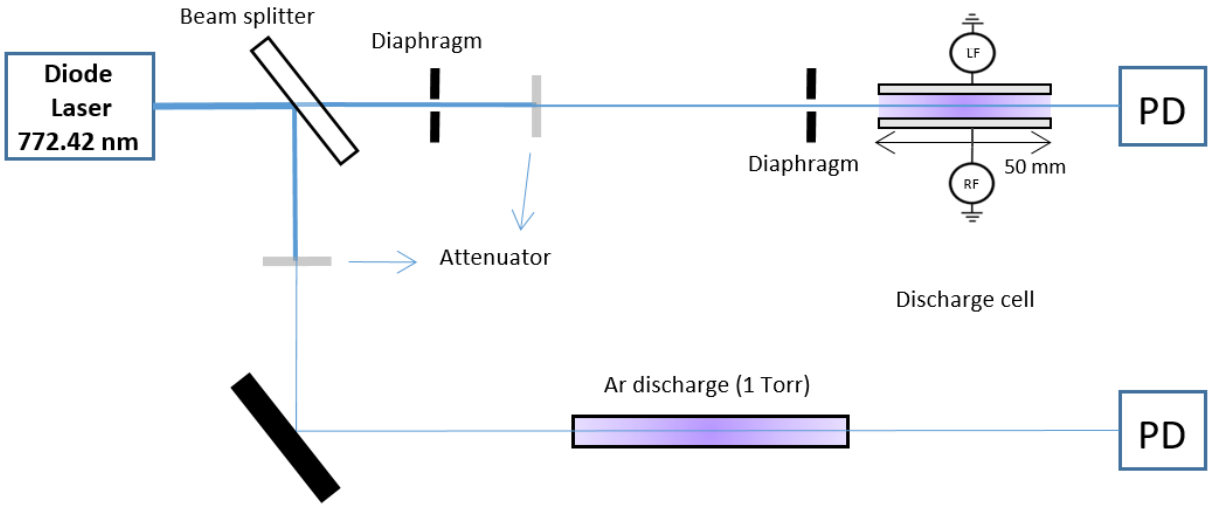



*Figure 2. Experimental setup used for determination of the population of Ar $1s_3$ atoms by absorption spectroscopy using a tunable diode laser. PD represents photodiodes.*

Figure 3 shows the full absorbance profile when the laser wavelength is scanned around the 772.4 nm range in Ar-based DBDs. Given the closeness of the 772.38 and 772.42 nm transitions, their pressure-broadened absorption profiles overlap under atmospheric pressure conditions. In addition, given the order of magnitude difference in their oscillator strengths (0.0278 and 0.314 for 772.38 and 772.42 nm lines, respectively [51]), the absorption peak intensity of the combined lines is located closer to 772.42 nm. The relative values of the two peak absorbance line profiles and their respective linewidths can be deduced by fitting the experimentally recorded absorbance with two Voigt functions, also shown in Figure 3 by black and red curves. Absolute number densities of metastable argon atoms can be deduced from their respective peak absorbance and width, as described in [48,50–53].

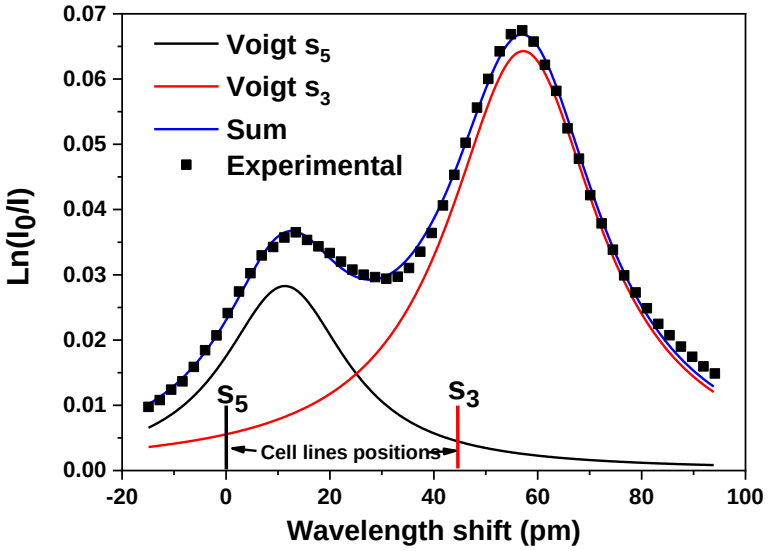



*Figure 3. Absorbance profile recorded around 772.4 nm in the Ar-based DBD. Black and red curves are absorbance profiles of 772.38 and 772.42 nm lines, respectively. Positions of these lines in the low-pressure Ar cell are indicated by* two *vertical lines (red and black for 772.38 and 772.42 nm lines, respectively).*

Here, the number density of metastable atoms as a function of time and space is obtained by setting the laser wavelength at the peak of the pressure broadened $1s_3$-$2p_2$ transition, which is shifted by about 13 pm from the vacuum wavelength of this line. Note that, the absorption signal from a low-pressure argon discharge cell (see Figure 2) [48,49] is used to tune the diode laser at the peak position of the $1s_3$-$2p_2$ transition. For both atmospheric-pressure DBD and low-pressure cell, the absorption signals are acquired with fast photodiodes (3.5 ns rise and fall times) and recorded with digital oscilloscope for data analysis and further data processing. In the DBD, the laser beam crosses the gas flow lines (perpendicular to the plan of Fig. 1) such that the absorption length is fixed to 50 mm (see Figure 2). Diaphragms, placed on the laser path before the discharge zone, reduce the laser beam diameter to about 0.5 mm. Spatially-resolved measurements in the 2 mm gap is obtained by moving simultaneously the laser beam, diaphragms system and detector in the inter-electrode space.

Figure 4 presents time-variation curves of the Ar($1s_3$) density recorded at two positions in the inter-electrode gap of the 50 kHz DBD operated in a homogeneous glow regime. In the first case, the laser beam was placed in the middle of the gap, while for the second one it was close to the upper electrode. Current-voltage characteristics are also shown for comparison. Here, data are presented for one full cycle of the applied LF voltage. In the first half-cycle, the top electrode is the cathode, while in the second one this electrode is the anode. As can be seen in Figure 4, a single discharge current peak appears per half cycle of the applied voltage; this is typical of the homogeneous DBDs operated in a

glow discharge regime [33,34]. Similar behaviors can be seen for both Ar($1s_3$) curves, with rise and decay times in the sub-microsecond time scale. Here, Ar($1s_3$) reaches a maximum value of 1.1 $10^{17}m^{-3}$ close to the cathode with 3.1 $10^{16}m^{-3}$ in the gas bulk. While similar trends and peak values arise in both half-cycles in the middle of the gap, a dissymmetry between the two half-cycles is observed near the upper electrode. More specifically, an order of magnitude larger density is observed when the top electrode is the cathode (first half-cycle), than when it becomes the anode (second half-cycle). Such dissymmetry is in very good agreement with the physics of Ar-based DBDs operated in a glow regime: i) high-energy electrons, needed for the production of excited argon atoms by electron-impact excitation of ground state Ar atoms, are mainly present inside and at the edge of the cathode sheath; ii) at atmospheric pressure, transport of Ar metastable atoms by diffusion is very slow [30,49,54,55] such that their density is directly linked to their local production and destruction rates.

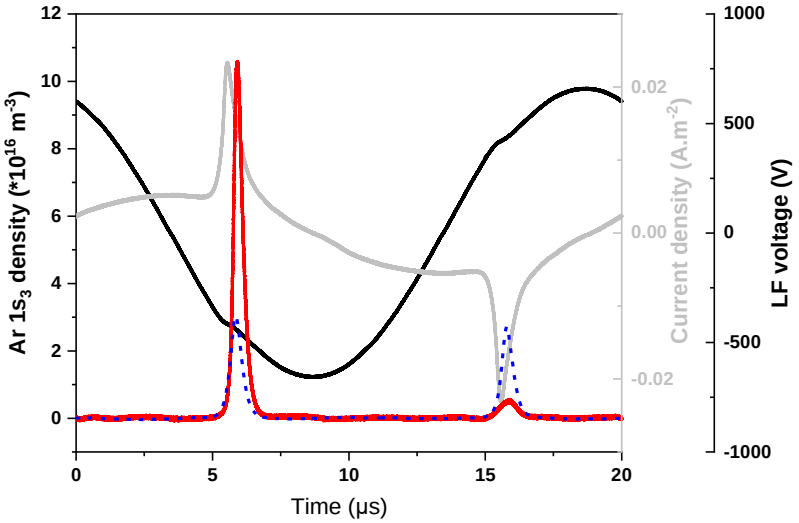



*Figure 4. Number density of Ar $1s_3$ atoms close to the upper electrode (solid) and in the middle of the gap (dash) over a complete cycle of the low frequency excitation (LF 650V, 50 kHz). Applied voltage (black) and total current density (grey, discharge + displacement current density) are also shown for comparison. On first half cycle of the applied voltage, the upper electrode is cathode while on the second half-cycle, the lower electrode is cathode.*

Figure 4 further shows that in both half-cycles, the maximum of the Ar metastable density near the cathode arises about 350 ns later than the discharge current peak (linked to the electron population), the delay being slightly shorter in the middle of the gap. This delay most likely results from the ~ 100 ns lifetime of Ar metastable atoms at 1 bar [56]. While the metastable and electron densities increase at the same time with the rise of the applied voltage, Ar metastable atoms tend to accumulate for a longer time than charged species (longer effective lifetimes) [30].

# 4. Kinetics driving metastable argon atoms

## 4.1 Fluid model from [25]

For a better understanding of the physics driving plane-to-plane Ar-based DBD sustained by either LF or dual frequency excitations, a 1D fluid model was recently developed by Magnan *et al.* [25]. This model solved the continuity and momentum equations for electrons, argon ions ($Ar^+$ and $Ar_2^+$) and excited argon 1s atoms as well electron energy balance equation. Here, even if Ar has four Ar 1s levels, $Ar(1s_2)$, $Ar(1s_3)$, $Ar(1s_4)$ and $Ar(1s_5)$, they are treated as a single Ar(1s) state [57–59] (see additional details below). These above cited equations were coupled to Poisson's equation for the electrical potential and to the standard reaction set displayed in Table 1 for selected collisional and radiative processes in Ar plasmas at atmospheric pressure. Boundary conditions were defined with a secondary electron emission coefficient $\gamma$, which describes the probability that an Ar(1s) particle or $Ar_2^+$ ion creates a secondary electron when interacting with the dielectric surfaces of the DBD cell. In [25], $\gamma$ was set to 0.1 for ions ($Ar^+$ and $Ar_2^+$) and Ar(1s) atoms. It is worth highlighting that in atmospheric-pressure plasmas for which $Ar^+$ conversion to $Ar_2^+$ is very fast, the contribution of $Ar_2^+$ completely dominates the ones of $Ar^+$ and Ar(1s).

| | Reaction | Rate coefficient | Ref |
|---|---|---|---|
| R1) | $e + Ar \rightarrow e + Ar(1s)$ | f(Te) | [60] |
| R2) | $e + Ar(1s) \rightarrow 2e + Ar^+$ | f(Te) | [60] |
| R3) | $e + Ar \rightarrow 2e + Ar^+$ | f(Te) | [60] |
| R4) | $e + Ar \rightarrow e + Ar$ | f(Te) | [60] |
| R5) | $e + Ar \rightarrow e + Ar(>1s)$ | f(Te) | [60] |
| R6) | $Ar^+ + 2Ar \rightarrow Ar_2^+ + Ar$ | $2.5*10^{-43}$ $m^6.s^{-1}$ | [45][61] |
| R7) | $e + Ar_2^+ \rightarrow Ar(1s) + Ar$ | $7.4*10^{-14}*Te^{-0.67}$ $m^3.s^{-1}$ | [62] |
| R8) | $Ar^+ + cathode \rightarrow e + Ar$ | $\gamma_{i\,(Ar+)}=0.1$ | [25] |
| R9) | $Ar_2^+ + cathode \rightarrow e + Ar$ | $\gamma_{i\,(Ar2+)}=0.1$ | [25] |
| R10) | $Ar(1s) + cathode \rightarrow e + Ar$ | $\gamma_{m\,(1s)}=0.1$ | [25] |
| R11) | $Ar(1s) + (NH_3) \rightarrow e + Ar^+ +$ (products) | $4.2*10^{-17}$ $m^3.s^{-1}$ | [63] |
| R12) | $Ar(1s) \rightarrow Ar$ | $1.5*10^6$ $s^{-1}$ | [64] |

*Table 1. Set of gas-phase and surface reactions used in the 1D model of [25]. Here Te is in K.*

Note that, the contribution of the 200 ppm of $NH_3$ present in the nominally pure argon gas, which leads to complex Ar-$NH_3$ interactions, was not explicitly introduced in the fluid model. Instead, two fictive reactions were included in Table 1: reaction R11) accounted for the primary electron production by Penning ionization of $NH_3$ by Ar(1s) atoms and reaction R12) accounted for the destruction of Ar(1s) atoms by collisions with Ar atoms and $NH_3$. The rate coefficients of reaction R11) was taken from [63]. As for the frequency of reaction R12), it was set to the value reported in Table 1 by adjusting the predictions of the model with the measured power, mean and maximal values of the Ar metastable densities [25].

To assess the correctness of this kinetic scheme for time-resolved measurements of Ar metastable atoms, we started by comparing the measured densities of Ar($1s_3$) atoms to the outcome of the model developed in [25]. For such experimental-model comparison, modelling data were integrated over a 0.5 mm circular region to match the laser beam diameter in the experiments. The comparison was realized with data sets recorded close to the upper electrode, although similar findings were found near the lower electrode of the DBD (not shown). Figure 5a presents the values obtained during a complete cycle of the applied voltage at 50 kHz. Clearly, the model [25] predicts much slower kinetics than the one seen in the experiment, both on the rising and falling side. A similar departure between the model and the experiment can be seen in Figure 5b for the dual-frequency DBD (LF 50 kHz, RF 5 MHz) in the $\alpha$-$\gamma$ mode [25,47]. Since reactions R1) to R10) presented in Table 1 are well-established in literature, such disagreement most likely results from the fictive reactions R11) and R12) representing the Penning effect, which are both involving Ar(1s) atoms.

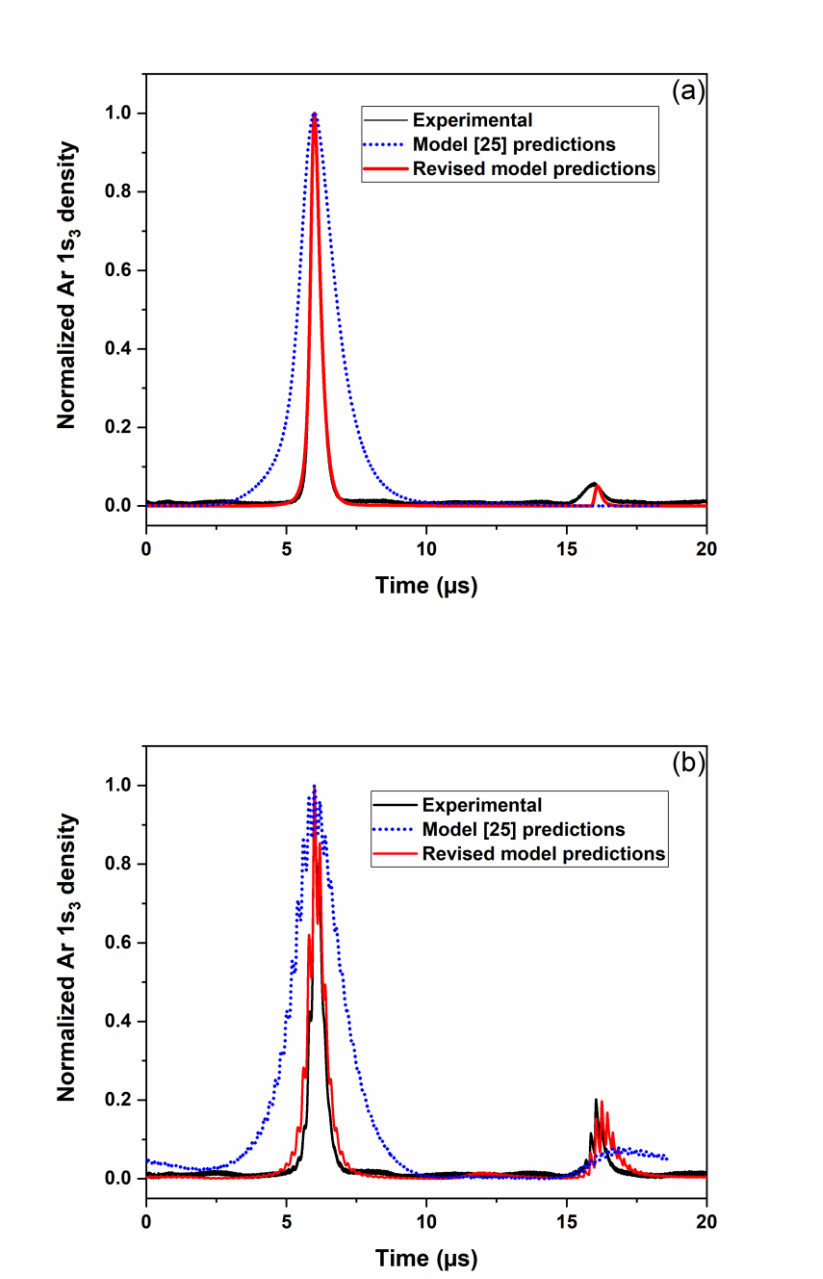



*Figure 5. Temporal evolution of the Ar(1s) number density (normalized values): measurements (in black), calculated with the fluid model of [25] (in blue) and with the revised fluid model (in red). The results are shown close to the upper electrode (which was at negative LF voltage in the first half-period and positive in the 2nd one) for (a) 50 kHz LF glow DBD and (b) dual-frequency RF + LF DBD in α-γ mode.*

## 4.2 Revised fluid model

In line with the findings of Figure 5, reactions R1) to R10) of Table 1 were maintained and fictive reactions R11) and R12) were reconsidered to more explicitly differentiate the contributions of Penning ionization, Penning dissociation, and 3-body conversion of Ar(1s) states. In addition to the creation of Ar excited dimers through 3-body reactions involving Ar(1s) atoms, the loss of $Ar_2$* by VUV photons and the VUV-induced secondary electron emission were also added; this yields to the revised kinetic scheme presented in Table 2.

| | | | | |
|---|---|---|---|---|
| (R13) | Ar(1s) + $NH_3$ ➔ products + Ar | | $5.4*10^{-16}$ $m^3.s^{-1}$ | [65] |
| | (R14) | Ar(1s) + ($NH_3$) ➔ $Ar^+$ + e + (products) | $2.3*10^{-16}$ $m^3.s^{-1}$ | [65], [64] |
| | (R15) | Ar(1s) + ($NH_3$) ➔ Ar + (products) | $3.1*10^{-16}$ $m^3.s^{-1}$ | [65], [64] |
| (R16) | Ar(1s) + 2Ar ➔ $Ar_2$* + Ar | | $1.1*10^{-44}$ $m^6.s^{-1}$ | [55] |
| (R17) | $Ar_2$* ➔ 2Ar + hv (VUV) | | $6.0*10^7$ $s^{-1}$ | [43], [61] |
| (R18) | hv (VUV) + wall ➔ e + wall | | $\gamma_{ph}$=0.1 | [46] |

*Table 2. Additional reactions involving excimers and photoemission. (R13) is not explicitly included but introduced through reactions (R14) and (R15), corresponding to Penning ionization and dissociation of $NH_3$, respectively. Note that, no population kinetics for $NH_3$ is introduced in the model: there, (R14) and (R15) frequencies are calculated for 40 ppm of $NH_3$.*

Reaction R13) corresponds to the total quenching reaction of Ar($1s_5$) metastable atoms by $NH_3$. In the revised version of the model, it is decomposed in R14) and R15). Considering the total quenching reaction rate of $5.4x10^{-16}$ $m^3.s^{-1}$ for R13), measured in [65], and the branching ratio of 0.42 for R14), measured in [64], this yields to a reaction rate for Penning ionization of $2.3x10^{-17}$ $m^3.s^{-1}$. Similarly, for $NH_3$ dissociation by Ar($1s_5$), the branching ratio is 0.58 [64], which yields to a reaction rate for R15) of $3.1x10^{-17}$ $m^3.s^{-1}$. Note that, these measured values differ by about a factor of 5 with respect to the one estimated in [63] and previously used for R11) in [25]. Over the range of experimental conditions investigated in this work, 200 ppm of $NH_3$ are injected in the nominally pure argon gas. However, upon discharge ignition, many reaction pathways lead to a significant decrease of this concentration [61]. Inspired by typical precursor fragmentation levels along the gas flow lines of DBD measured in similar

conditions by infrared absorption [66] or operated in various discharge modes [15,67,68], all data were obtained assuming a concentration fraction of 40 ppm.

Reaction R16) corresponds to the 3-body conversion of Ar(1s) atoms leading to excited argon dimers $Ar_2$* [69]. This state decays to the dissociative ground state of $Ar_2$ by producing the VUV continuum emission centered at 126 nm (reaction R17)) [56,61]. Here, the rate coefficient of R16) corresponds to the one measured for Ar($1s_5$) [55], and was extended to other Ar(1s) levels in agreement with Arakoni [61]. These VUV photons cannot be absorbed by Ar atoms or $Ar_2$ in its ground state and by the small amount of $NH_3$ (optically thin medium) [43]; hence, VUV photons have a long mean free path in the DBD cell (typically ~50 cm [45], i.e. 250 times greater than the inter-electrode gap). Consequently, they can rapidly reach the surface of the dielectric walls, inducing secondary electron emission [46]. The yield for such reaction, $\gamma_{ph}$, is assumed comparable to the one of ions and Ar(1s) atoms (R17)) in Table 2. Note that, $\gamma_{ph}$ includes the contributions of both direct, VUV-induced electron emission and VUV-induced desorption of electrons bound to the plasma-exposed dielectrics by weak polarization interactions [70–73]. In addition, photons are described with an infinite speed: photoemission is therefore instantaneous after the spontaneous dissociation of $Ar_2$*. Due to the small inter-electrode gap with respect to the electrode surface, it can be assumed that half of the photons reaches the cathode, the other half goes to the anode [46].

It is worth highlighting that the measurements examine the population of Ar($1s_3$), while the model considers all four Ar(1s) state as a block. To note; when accounting for the about 10 times lower oscillator strength of the 772.38 nm line, compared to the one of the 772.42 nm line, Figure 3 reveals that the number density of metastable atoms is about 5 times lower in the Ar($1s_3$) state than in the Ar($1s_5$) one. This is the ratio between the 2J+1 statistical weights of these states, which have angular momentum J=0 and 2, respectively [51]. A similar rule can be invoked to describe the populations of the resonant Ar($1s_2$) and Ar($1s_4$) states. According to the resonance radiation trapping theory of Holstein [74,75], extended by Walsh [76], the apparent lifetimes of these states in a 2 mm thick slab of atmospheric-pressure argon gas are 1.2 and 5 µs [44], respectively, which are about 100 times longer than the radiative lifetimes of these states [51]. However, due to the 3-body reaction with two ground state Ar atoms (described by R16)), and to the quenching by $NH_3$ (described by the sum of R14) and R15)), the effective lifetime of the four Ar(1s) states, metastable as well as resonance states, decreases by at least one order of magnitude (≈ 100 ns). Considering comparable rate coefficients reported for different Ar(1s) states for R13) in [65] and for R16) in [55], the population densities of these states become proportional to their respective production rates by electron impact excitation, which follow their respective statistical weights 2J+1. Moreover, population transfers between the four Ar(1s) states, induced by collisions with Ar atoms [55,77] and electrons [57,58], help for the

establishment of this statistical population distribution. Hence, the angular momentum J being 1, 0, 1 and 2 for Ar($1s_2$), Ar($1s_3$), Ar($1s_4$) and Ar($1s_5$) states, respectively [51], their relative population densities should follow 3:1:3:5 ratios. Hence, the total density of excited argon atoms in the four Ar(1s) states calculated by the model corresponds to 12 times the measured density of the Ar($1s_3$) level.

Revised values of the normalized metastable number densities are presented in Figure 5a for the LF discharge (50 kHz) and dual-frequency DBD (LF 50 kHz, RF 5 MHz) operated in the α-γ mode [25,47]. Clearly, much better agreement is observed with the revised version of the model than with the one originally developed by Magnan *et al.* [25]. Hence, in addition to the higher reaction rates for Penning ionization and dissociation (R14) and R15)), the fast creation of $Ar_2$* R16) and its rapid radiative decay, leading to VUV emission and secondary electron emission (R17) and R18)), allow a much better description of the time variation of Ar(1s) populations in both LF and LF-RF DBDs, with much more prominent rise and decay times.

A very small peak of Ar(1s) also appears in Figure 5 close to the anode when $Ar_2$* and photoemission resulting from VUV photons are included in the model. This aspect was examined in more details by plotting the Ar(1s) mapping over time and space. Results are presented in Figure 6a. One can see that the maximum of Ar(1s) is close to the cathode, but the high-density area extends into the gap and reappears close to the anode. Over the range of experimental conditions investigated, Ar(1s) atoms are mainly created by R1), i.e. by high-energy electrons [25], and transport by diffusion is negligible [30,49,54,55]. Spatial variation of the electric field along the gap when the population of Ar(1s) species increases at the anode are presented in Figure 6b with and without chain reactions leading to the photoemission by VUV photons. Compared to [25], the revised kinetic scheme used in the fluid model leads to an increase of the electric field in the gas bulk and near the anode. This necessarily implies a more prominent electron drift from the cathode to the anode and thus a more important creation of Ar(1s) atoms by high-energy electrons in the anode region.

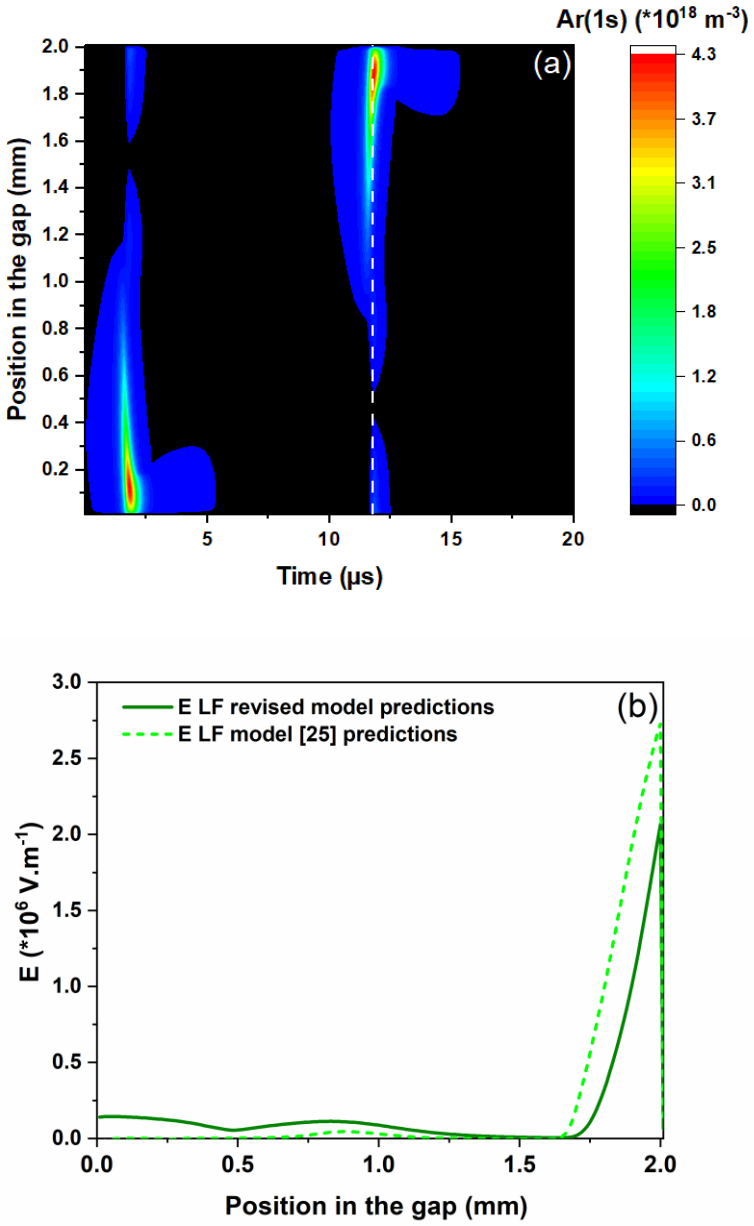



*Figure 6. a) Ar(1s) number density evolution over space and time in the LF DBD, b) spatial profile of the electric field along the gap when Ar(1s) is maximum at the anode (vertical line in a). In b), the results for the electric field are shown with the model used in [25] and with the revised version developed in this work.*

# 5. Consequences of excimer formation and photoemission on Ar-based DBDs in LF and LF-RF regimes

## 5.1. Discharge kinetics

The introduction of the population kinetics of $Ar_2$* (formation through reaction R16) and loss through reaction R17)) and photoemission by VUV photons (reaction R18)) strongly modify the physics driving Ar-based DBDs in both LF and LF-RF DBD regimes.

Table 3 summarizes important modifications on the dominant creation and loss terms of both Ar(1s) atoms and electrons. For Ar(1s), electron-impact excitation represents the dominant creation pathway in both LF and LF-RF regimes. As for the losses, Penning dissociation accounts for 88% of Ar(1s) consumption when using the reaction set provided by Magnan *et al.* [25]. In the revised model, over the range of experimental conditions investigated, the contribution of Penning dissociation decreases, and the dominant loss mechanism becomes the creation of $Ar_2$*. In the same way, consumption of Ar(1s) states for Penning ionization also reduces. In line with these results, one may think that the more prominent rise and decay times observed for the population of metastable argon atoms in Figure 5a and Figure 5b with the revised model is entirely linked to the $Ar_2$* kinetics, and not to photoemission. However, if R18) is removed from the model, discharge breakdown no longer occurs, even for very high amplitudes of the LF voltage. This feature is obviously due to the high loss rates of Ar(1s) atoms, which can no longer bring energy to the discharge. It also shows that the creation of Ar(1s) atoms is largely related to photoemission.

| | | 50 kHz LF | | 50 kHz LF + 5 MHz RF | |
|---|---|---|---|---|---|
| | | Model of [25] | Revised model | Model of [25] | Revised model |
| Creation of Ar(1s) | e-$Ar_2^+$ recombination (%) | 4 | <0.1 | 1 | <0.1 |
| | Direct excitation (%) | 96 | 100 | 99 | 100 |
| Ar (1s) losses | To the walls (%) | <0.1 | <0.1 | <0.1 | <0.1 |
| | Penning ionization (%) | 12 | 3 | 12 | 3 |
| | $NH_3$ dissociation (%) | 88 | 4 | 88 | 4 |
| | Creation of the dimer Ar2* (%) | -- | 93 | -- | 93 |
| Creation of $e^-$ | Penning ionization (%) | 79 | 49 | 82 | 52 |
| | Direct ionization (%) | 14 | 30 | 9 | 23 |
| | Secondary emission (%) | 7 | 21 | 9 | 25 |
| $e^-$ losses | To the walls (%) | 76 | 92 | 94 | 98 |
| | e-ion recombination (%) | 24 | 8 | 6 | 2 |

*Table 3 Space- and time-averaged contribution of the different mechanisms to the creation and loss of Ar(1s) and electrons for LF 50 kHz 1000 V and dual-frequency 50kHz 750 V + 5MHz 350 V*

As for the electrons,

Table 3 shows that while Penning and direct ionization were the dominant ionization pathways in the initial model [25,47], about 3 times more electrons are now created by photoemission at the walls with the addition of the $Ar_2$* kinetics and photoemission (R15)). However, the contribution of Penning ionization remains larger than the one of Ar direct ionization. As said previously, even if only 3% of Ar(1s) consumption are involved in Penning ionization, this reaction remains necessary for the discharge ignition. If Penning ionization is entirely removed from the revised model, the discharge no longer ignites, which fully supports previous experimental findings demonstrating the importance of

the $NH_3$ Penning gas mixture in the physics driving Ar-based, low-frequency DBDs [18,23]. Experimentally, in dual-frequency DBDs, the $\gamma$ mode is never reached without $NH_3$ and thus without Penning ionization contributions. Since direct ionization of $NH_3$ is fully negligible over the range of experimental conditions investigated [61], this must be linked to Penning ionization contributions.

Table 3 further reveals that the relative contribution of electron losses to the walls increases with respect to recombination processes in the bulk. The explanation is that with addition of the $Ar_2$* kinetics and photoemission, the contribution of secondary electrons increases, creating more ions and electrons in the sheath. Ions are thus more effectively lost to the cathode surface, while electrons can more easily drift to the anode surface.

## 5.2.RF α ➔ RF α–γ transition criterion in dual frequency RF-LF

In LF-RF Ar-$NH_3$ DBDs, a transition from α to α-γ can occur with the increase of the LF voltage [25,47]. Under atmospheric pressure conditions, the first mode is called α or Ω mode, and is characterized by an ohmic heating and electron energy dissipation in the bulk [20,22]. The second mode is called α-γ mode: during each half cycle of the LF voltage, electron Joule heating and electron energy loss reach a maximum in the sheath region for some µs [78]. This transient γ mode is observed when the gas voltage amplitude reaches a high enough value. Like in a LF DBD, when the γ mode is reached, the gas voltage decreases due to the charge of the dielectrics. Consequently, the maximum of the gas voltage is observed just after the transition from α to γ mode, and the γ mode duration is limited [20,47]. In this γ mode, the contribution of secondary electrons to the gas ionization becomes large enough to reach the self-sustainment criterion in the cathode sheath [47,79]:

$$\frac{\gamma_i \langle \Gamma_{i,sheath} \rangle_{RF}}{\langle \Gamma_{SEE} \rangle_{RF}} > 1\,, \tag{1}$$

where $\langle \Gamma_{i,Sheath} \rangle_{RF}$ is the maximum value at a given time of the LF voltage of the total ion flux through electron Joule heating and electron multiplication in the cathode sheath [47]

$$\Gamma_{i,sheath}(t) = \int_{cathode}^{sheath\ edge} S_i(x,t)dx\,, \tag{2}$$

where $S_i$ is the volume production rate of ions. In Equation (2), the integration is realized over the sheath thickness (In practice, this is done by means of a weighting function defined as $W(x) = 1 - ne(x)/ni(x)$, which varies smoothly from ≈1 at the wall to ≈0 in the plasma bulk; the source term $S_i$ is then multiplied by W(x) and then integrated from the electrode to the center of the plasma, as explained in [47]). As for $\langle \Gamma_{SEE} \rangle_{RF}$ in Equation (1), it corresponds to the maximum at a given time of the LF voltage of the secondary electron flux emitted from the cathode wall in the DBD cell. Note that, the criterion given by Equation (1) is obtained with values averaged over one RF cycle because the self-sustainment criterion involving ion transport back to the wall is too slow to react to the RF fluctuations of the electric field in the sheath [47]. Generally, the transition from α to α-γ mode is related to secondary electron emission by ion bombardment only ($\gamma_i$); in line with the findings of this work, the secondary electron emission contribution by photons ($\gamma_{ph}$) must be added such that the self-sustainment criterion becomes

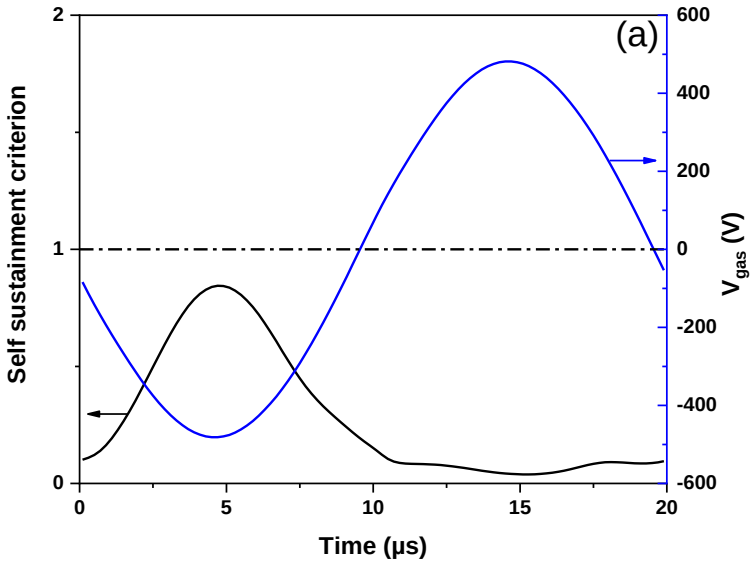
$$\frac{\gamma_i \langle \Gamma_{i,sheath} \rangle_{RF} + \frac{1}{2}\gamma_{ph}\eta \langle \Gamma_{Ar(1s),sheath} \rangle_{RF}}{\langle \Gamma_{SEE} \rangle_{RF}} > 1, \quad (3)$$

where $\langle \Gamma_{Ar(1s),sheath} \rangle_{RF}$ is the maximum value at a given time of the LF voltage of the Ar(1s) flux in the cathode sheath

$$\Gamma_{Ar(1s),sheath}(t) = \int_{cathode}^{sheath\ edge} S_{Ar(1s)}(x,t)dx\,, \quad (4)$$

where $S_{Ar(1s)}$ is the volume production rate of Ar(1s). In Equation (3), $\eta$ corresponds to the fraction of the argon metastable atoms in the sheath that lead to the creation of $Ar_2$* and then to VUV photons. Over the range of experimental conditions investigated, with the reaction set presented in Table 2, η is approximately constant ($\eta \cong 0.926$) due to the constant frequencies of all the dominant conversion processes of Ar(1s). It follows that the maximum photon flux in the sheath is directly proportional to the maximum Ar(1s) flux in the sheath. Since $\eta \langle \Gamma_{Ar(1s),sheath} \rangle_{RF}$ includes photons produced in the cathode sheath but towards both the anode and the cathode, the ½ factor in Equation (3) accounts for the fact that, in optically thin media for VUV photons, only half of the photons reaches the cathode (the other half reaches the anode).

Figure 7 presents the self-sustainment criterion calculated by the Equation (3) as a function of time during a LF period of the dual-frequency discharge. The results are shown for two amplitudes of the LF voltage: in (a), the LF voltage remains below the value required to induce a transition from α to γ mode, while in (b), the LF voltage is such that a transient γ mode occurs. Based on Equation (2), the discharge can transit to the γ mode if the self-sustainment criterion becomes greater than 1 over a given time frame of the LF voltage. In Figure 7 (a), this criterion is never satisfied whereas in Figure 7 (b), it is fulfilled between 0.85 and 2.5 µs. In such conditions, the sheath becomes self-sustained. The presence of the γ mode can be further confirmed by the gas voltage (averaged over one RF cycle) behaviors also displayed in Figure 7. While the gas voltage remains more or less sinusoidal in Figure 7 (a), a rapid gas voltage drop can be seen in Figure 7 (b) due to the corresponding charge of the dielectrics.



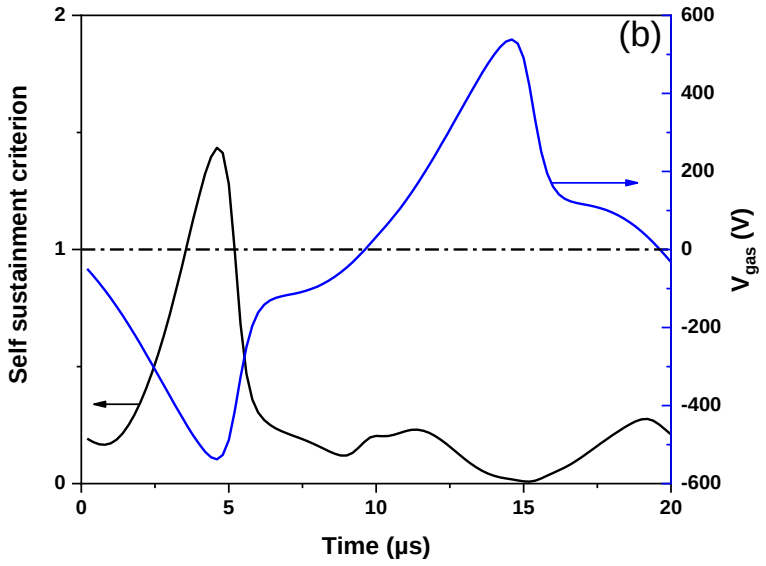



*Figure 7. Self-sustainment criterion plot as a function of time during a complete cycle of the LF voltage. Here, the criterion corresponds to left-hand-side of Equation (3) (in black). Gas voltage values are also shown (in blue). Results are presented for a dual frequency LF (50 kHz) – RF (5MHz), $V_{RF}$ = 350 V, (a) $V_{LF}$ = 600 V, (b) $V_{LF}$ = 650 V*

In this framework, Figure 8 presents the self-sustainment criterion, at the moment when $|V_{gas}|$ is maximum, calculated by the left-hand-side of Equation (3) as a function of the amplitude of the LF voltage. Again, when the ratio exceeds 1, i.e. when each secondary electron produces enough ions and Ar(1s) in the sheath to cause the emission of one or more new secondary electrons, the discharge transits to the γ mode, i.e. the sheath becomes self-sustained [25,47]. As can be seen, the transition occurs for different LF voltage amplitudes depending on the specific set of the chosen $\gamma_i$ and $\gamma_{ph}$ values. For $\gamma_i$=0.1, the minimum LF voltage required for the α-γ mode transition decreases as $\gamma_{ph}$ increases. Hence, for a more important electron production through photoemission, a lower LF voltage is sufficient to reach the number of ionizations provided by the self-sustainment criterion. On the other hand, Figure 8 shows that $\gamma_i$ has only little influence on the value of the LF voltage required for the transition. This is related to the long drift time of ions to the cathode compared to the γ mode duration, which limits the influence of $\gamma_{ions}$ on the α-γ transition voltage. More precisely, the ions drift from the sheath edge to the cathode lasts about 1 µs, which is the magnitude of the duration of the γ mode. Consequently, ions produced at the sheath edge during the γ mode only have little influence on the γ mode transition.

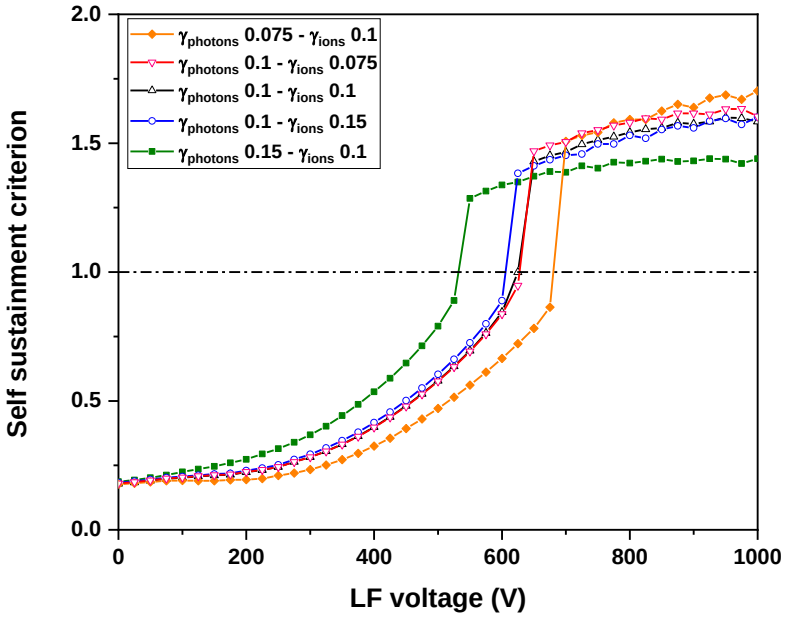



*Figure 8. Self-sustainment criterion plot as a function of the amplitude of the LF voltage in dual-frequency LF-RF DBDs. Here, the criterion corresponds to left-hand-side of Equation (3).The results are shown for various $\gamma_i$ and $\gamma_{ph}$ values.*

# 6. Conclusion

Through a comparison between the measured and simulated populations of metastable argon atoms, the objective of this work was to highlight the role of excimer formation, followed by the VUV emission and photoemission on the Ar metastable kinetics in Ar-$NH_3$ dielectric barrier discharges at atmospheric pressure. The model initially developed to describe Ar-based dual-frequency DBDs [25,47] was not able to reproduce the time variation of Ar(1s) atoms density characterized by rise and decay times in the microsecond time scale. On the other hand, including $Ar_2$* formation, $Ar_2$* spontaneous deexcitation leading to VUV continuum emission, and the induced photoemission at the walls, provided much more accurate Ar metastable kinetics for both low-frequency (50 kHz) and dual frequency (50 kHz - 5 MHz) excitations. In addition, the apparition of a peak in the density of metastable argon atoms at the anode was also better described using photoemission. It was shown that this peak of Ar(1s) atoms density is not directly linked to the consumption-creation balance of Ar(1s) atoms, but rather to the production of an electron beam passing through the discharge during the LF breakdown. $Ar_2$* and photoemission further played a significant role on the ionization kinetics : while Penning were the truly dominant ionization pathways in the initial model [25,47], the part of electron's creation by photoemission and direct ionization increases to become of the order of

magnitude of that of Penning ionization in the refined version of the model. Photoemission was also demonstrated to influence the transition from α to α-γ mode.

## 7. Acknowledgments

The work in France was supported by the Agence Nationale de la Recherche through the Investissement d'avenir program (ANR10LABX2201). As for the one in Canada, it was funded by the National Science and Engineering Research Council (NSERC RGPIN-2018-04550) and by the Fondation Courtois. The "Réseau des Plasmas Froids" of CNRS/MCRT (France) is acknowledged for providing the DFB diode laser and the travel support for Nader Sadeghi. All authors would like to acknowledge the financial support of the CNRS and Université de Montréal through their contributions to the International Research Network on Controlled Multifunctional Nanomaterials.

# References


[1] Morent R, De Geyter N, Gengembre L, Leys C, Payen E, Van Vlierberghe S and Schacht E 2008 Surface treatment of a polypropylene film with a nitrogen DBD at medium pressure *EPJ Applied Physics* vol 43 pp 289–94

[2] Borcia G, Anderson C A and Brown N M D 2003 Dielectric barrier discharge for surface treatment: Application to selected polymers in film and fibre form *Plasma Sources Sci. Technol.* **12** 335–44

[3] Merche D, Vandencasteele N and Reniers F 2012 Atmospheric plasmas for thin film deposition: A critical review *Thin Solid Films* **520** 4219–36

[4] Borcia G and Brown N M D 2007 Hydrophobic coatings on selected polymers in an atmospheric pressure dielectric barrier discharge *J. Phys. D. Appl. Phys.* **40** 1927–36

[5] Profili J, Rousselot S, Tomassi E, Briqueleur E, Aymé-Perrot D, Stafford L and Dollé M 2020 Toward More Sustainable Rechargeable Aqueous Batteries Using Plasma-Treated Cellulose-Based Li-Ion Electrodes *ACS Sustain. Chem. Eng.* **8** 4728–33

[6] Levasseur O, Stafford L, Gherardi N, Naudé N, Blanchard V, Blanchet P, Riedl B and Sarkissian A 2012 Deposition of Hydrophobic Functional Groups on Wood Surfaces Using Atmospheric-Pressure Dielectric Barrier Discharge in Helium-Hexamethyldisiloxane Gas Mixtures *Plasma Process. Polym.* **9** 1168–75

[7] Lelièvre J, Kafle B, Saint-Cast P, Brunet P, Magnan R, Hernandez E, Pouliquen S and Massines F 2019 Efficient silicon nitride SiNx:H antireflective and passivation layers deposited by atmospheric pressure PECVD for silicon solar cells *Prog. Photovoltaics Res. Appl.* **27** 1007–19

[8] Wang J J, Choi K S, Feng L H, Jukes T N and Whalley R D 2013 Recent developments in DBD plasma flow control *Prog. Aerosp. Sci.* **62** 52–78

[9] Enloe C L, McLaughlin T E, VanDyken R D, Kachner K D, Jumper E J and Corke T C 2004 Mechanisms and Responses of a Single Dielectric Barrier Plasma Actuator: Plasma Morphology *AIAA J.* **42** 589–94

[10] Michielsen I, Uytdenhouwen Y, Pype J, Michielsen B, Mertens J, Reniers F, Meynen V and Bogaerts A 2017 CO2 dissociation in a packed bed DBD reactor: First steps towards a better understanding of plasma catalysis *Chem. Eng. J.* **326** 477–88

[11] McAdams R 2001 Prospects for non-thermal atmospheric plasmas for pollution abatement *J. Phys. D. Appl. Phys.* **34** 2810–21

[12] Ono R and Oda T 2007 Ozone production process in pulsed positive dielectric barrier discharge *J. Phys. D. Appl. Phys.* **40** 176–82

[13] Mericam-Bourdet N, Kirkpatrick M J, Tuvache F, Frochot D and Odic E 2012 Effect of voltage waveform on dielectric barrier discharge ozone production efficiency *Eur. Phys. J. Appl. Phys.* **57** 30801

[14] Ulrich Kogelschatz 2003 Dielectric-Barrier Discharges: Their History, Discharge Physics, and Industrial Applications *Plasma Chem. Plasma Process.* **23** 1–46

[15] Massines F, Sarra-Bournet C, Fanelli F, Naudé N and Gherardi N 2012 Atmospheric pressure low temperature direct plasma technology: Status and challenges for thin film deposition

*Plasma Process. Polym.* **9** 1041–73

[16] Kogelschatz U 1987 Filamentary and diffuse barrier discharges *J. Phys. D Appl. Phys* **20** 1421

[17] Kogelschatz U 2002 Filamentary, patterned, and diffuse barrier discharges *IEEE Trans. Plasma Sci.* **30** 1400–8

[18] Bazinette R, Subileau R, Paillol J and Massines F 2014 Identification of the different diffuse dielectric barrier discharges obtained between 50kHz to 9MHz in Ar/NH3 at atmospheric pressure *Plasma Sources Sci. Technol.* **23** 035008

[19] Boisvert J, Stafford L, Naudé N, Margot J and Massines F 2018 Electron density and temperature in an atmospheric-pressure helium diffuse dielectric barrier discharge from kHz to MHz *Plasma Sources Sci. Technol.* **27** 035005

[20] Shi J J and Kong M G 2005 Mechanisms of the α and γ modes in radio-frequency atmospheric glow discharges *J. Appl. Phys.* **97** 023306

[21] Walsh J L, Shi J J and Kong M G 2006 Contrasting characteristics of pulsed and sinusoidal cold atmospheric plasma jets *Appl. Phys. Lett.* **88** 171501

[22] Shi J J and Kong M G 2007 Mode transition in radio-frequency atmospheric argon discharges with and without dielectric barriers *Appl. Phys. Lett.* **90** 101502

[23] Bazinette R, Sadeghi N and Massines F 2020 Dual frequency DBD: Influence of the amplitude and the frequency of applied voltages on glow, Townsend and radiofrequency DBDs *Plasma Sources Sci. Technol.* **29** 095010

[24] Liu Y, Van'T Veer K, Peeters F J J, Mihailova D B, Van Dijk J, Starostin S A, Van De Sanden M C M and De Vries H W 2018 Numerical simulation of atmospheric-pressure 200 kHz/13.56 MHz dual-frequency dielectric barrier discharges *Plasma Sources Sci. Technol.* **27** 105016

[25] Magnan R, Hagelaar G, Chaker M and Massines F 2020 Atmospheric pressure dual RF-LF frequency discharge: Influence of LF voltage amplitude on the RF discharge behavior *Plasma Sources Sci. Technol.* **29** 035009

[26] Park S, Choe W, Moon S Y and Shi J J 2018 Electron Information in Single-And Dual-Frequency Capacitive Discharges at Atmospheric Pressure *Sci. Rep.* **8** 1–10

[27] Brunet P, Rincón R, Matouk Z, Chaker M and Massines F 2018 Tailored Waveform of Dielectric Barrier Discharge to Control Composite Thin Film Morphology *Langmuir* **34** 1865–72

[28] Profili J, Levasseur O, Naudé N, Chaneac C, Stafford L and Gherardi N 2016 Influence of the voltage waveform during nanocomposite layer deposition by aerosol-assisted atmospheric pressure Townsend discharge *J. Appl. Phys.* **120** 053302

[29] Zhang Z, Nie Q, Wang Z and Lim J W M 2020 Selective modulation of plasma parameters in an atmospheric dielectric barrier discharge driven by sawtooth-type tailored voltage waveforms *Phys. Plasmas* **27** 063519

[30] Lymberopoulos D P and Economou D J 1993 Fluid simulations of glow discharges: Effect of metastable atoms in argon *J. Appl. Phys.* **73** 3668–79

[31] Dilecce G, Ambrico P F, Benedictis S De and De Benedictis S 2007 N2(A3Σ uu density measurement in a dielectric barrier discharge in N2 and N2 with small O2 admixtures *Plasma Sources Sci. Technol.* **16** 511–22

[32] Tyl C, Lin X, Bouzidi M C, Dap S, Caquineau H, Ségur P, Gherardi N and Naudé N 2018 Investigation of memory effect in atmospheric pressure dielectric barrier discharge in nitrogen with small oxygen or nitric oxide addition *J. Phys. D. Appl. Phys.* **51** 354001

[33] Massines F, Rabehi A, Decomps P, Gadri R B, Ségur P and Mayoux C 1998 Experimental and theoretical study of a glow discharge at atmospheric pressure controlled by dielectric barrier *J. Appl. Phys.* **83** 2950–7

[34] Massines F, Ségur P, Gherardi N, Khamphan C and Ricard A 2003 Physics and chemistry in a glow dielectric barrier discharge at atmospheric pressure: diagnostics and modelling *Surf. Coatings Technol.* **97** 719–22

[35] Massines F, Gherardi N, Naudé N and Ségur P 2005 Glow and Townsend dielectric barrier discharge in various atmosphere *Plasma Phys. Control. Fusion* **47** B577–B588

[36] Massines F, Gherardi N, Naudé N and Ségur P 2009 Recent advances in the understanding of homogeneous dielectric barrier discharges *EPJ Appl. Phys.* **47** 22805

[37] Desjardins E, Laurent M, Durocher-Jean A, Laroche G, Gherardi N, Naudé N and Stafford L 2018 Time-resolved study of the electron temperature and number density of argon metastable atoms in argon-based dielectric barrier discharges *Plasma Sources Sci. Technol.* **27** 015015

[38] Moselhy M, Petzenhauser I, Frank K and Schoenbach K H 2003 Excimer emission from microhollow cathode argon discharges *J. Phys. D. Appl. Phys.* **36** 2922–7

[39] Foest R, Bindemann T, Brandenburg R, Kindel E, Lange H, Stieber M and Weltmann K-D 2007 On the Vacuum Ultraviolet Radiation of a Miniaturized Non-thermal Atmospheric Pressure Plasma Jet *Plasma Process. Polym.* **4** S460–4

[40] Lange H, Foest R, Schafer J and Weltmann K-D 2009 Vacuum UV Radiation of a Plasma Jet Operated With Rare Gases at Atmospheric Pressure *IEEE Trans. Plasma Sci.* **37** 859–65

[41] Andrew Y, Abraham I, Booske J H, Lu Z C and Wendt A E 2000 Absolute densities of long lived species in an ionized physical vapor deposition copper-argon plasma *J. Appl. Phys.* **88** 3208–19

[42] Liu F, Nie L, Lu X, Stephens J and Ostrikov K 2020 Atmospheric plasma VUV photon emission *Plasma Sources Sci. Technol.* **29** 065001

[43] Gellert B and Kogelschatz U 1991 Generation of excimer emission in dielectric barrier discharges *Appl. Phys. B Photophysics Laser Chem.* **52** 14–21

[44] Boffard J B, Lin C C, Culver C, Wang S, Wendt A E, Radovanov S and Persing H 2014 Comparison of surface vacuum ultraviolet emissions with resonance level number densities. I. Argon plasmas *J. Vac. Sci. Technol. A Vacuum, Surfaces, Film.* **32** 021304

[45] Lam S K, Zheng D, Lo A, Dem'yanov A and Napartovich A P 2000 Kinetics of Ar2* in high-pressure pure argon *J. Phys. D. Appl. Phys.* **33** 242–51

[46] Phelps A V. and Petrović Z L 1999 Cold-cathode discharges and breakdown in argon: surface and gas phase production of secondary electrons *Plasma Sources Sci. Technol.* **8** R21

[47] Magnan R, Hagelaar G, Chaker M and Massines F 2021 Atmospheric pressure dual RF – LF frequency discharge : transition from α to α – γ -mode *Plasma Sources Sci. Technol.* **30** 015010

[48] Hübner S, Sadeghi N, Carbone E A D and Van Der Mullen J J A M 2013 Density of atoms in Ar*(3p(5)4s) states and gas temperatures in an argon surfatron plasma measured by tunable

laser spectroscopy *J. Appl. Phys.* **113** 143306

[49] Durocher-Jean A, Desjardins E and Stafford L 2019 Characterization of a microwave argon plasma column at atmospheric pressure by optical emission and absorption spectroscopy coupled with collisional-radiative modelling *Phys. Plasmas* **26** 063516

[50] Niermann B, Böke M, Sadeghi N and Winter J 2010 Space resolved density measurements of argon and helium metastable atoms in radio-frequency generated He-Ar micro-plasmas *Eur. Phys. J. D* **60** 489–95

[51] P.J. Linstrom and W.G. Mallard E NIST Chemistry WebBook, NIST Standard Reference Database Number 69, National Institute of Standards and Technology, Gaithersburg MD, 20899 *NIST Chem. Webb.*

[52] Douat C, Kacem I, Sadeghi N, Bauville G, Fleury M and Puech V 2016 Space-time resolved density of helium metastable atoms in a nanosecond pulsed plasma jet: Influence of high voltage and pulse frequency *J. Phys. D. Appl. Phys.* **49** 285204

[53] Sadeghi N, Magnan R and Massines F Pressure broadening of 772.376 and 772.421 nm argon lines and kinetics of argon metastable atoms [To be submitted]

[54] Belostotskiy S G, Donnelly V M, Economou D J and Sadeghi N 2009 Spatially resolved measurements of argon metastable (1s5) density in a high pressure microdischarge using diode laser absorption spectroscopy *IEEE Trans. Plasma Sci.* **37** 852–8

[55] Nayak G, Simeni Simeni M, Rosato J, Sadeghi N and Bruggeman P J 2020 Characterization of an RF-driven argon plasma at atmospheric pressure using broadband absorption and optical emission spectroscopy *J. Appl. Phys.* **128** 243302

[56] Kolts J H and Setser D W 1978 Decay rates of Ar(4s,3P2), Ar(4s', 3P0), Kr(5s,3P2), and Xe(6s, 3P2) atoms in argon *J. Chem. Phys.* **68** 4848–59

[57] Carbone E, Van Veldhuizen E, Kroesen G and Sadeghi N 2015 Electron impact transfer rates between metastable and resonant states of argon investigated by laser pump-probe technique *J. Phys. D. Appl. Phys.* **48** 425201

[58] Carbone E, Hübner S, Van Der Mullen J J A M, Kroesen G M W and Sadeghi N 2013 Determination of electron-impact transfer rate coefficients between argon 1s2 and 1s3 states by laser pump-probe technique *J. Phys. D. Appl. Phys.* **46** 415202

[59] Carbone E, Sadeghi N, Vos E, Hübner S, Van Veldhuizen E, Van Dijk J, Nijdam S and Kroesen G 2015 Spatio-temporal dynamics of a pulsed microwave argon plasma: Ignition and afterglow *Plasma Sources Sci. Technol.* **24** 015015

[60] Hagelaar G J M and Pitchford L C 2005 Solving the Boltzmann equation to obtain electron transport coefficients and rate coefficients for fluid models *Plasma Sources Sci. Technol.* **14** 722–33

[61] Arakoni R A, Bhoj A N and Kushner M J 2007 H2 generation in Ar/NH3 microdischarges *J. Phys. D. Appl. Phys.* **40** 2476–90

[62] Mehr F J and Biondi M A 1968 Electron-temperature dependence of electron-ion recombination in Argon *Phys. Rev.* **176** 322–6

[63] Kushner M J 1992 Simulation of the gas-phase processes in remote-plasma-activated chemical-

vapor deposition of silicon dielectrics using rare gas-silane-ammonia mixtures *J. Appl. Phys.* **71** 4173–89

[64] Balamuta J, Golde M F and Ho Y 1983 Product distributions in the reactions of excited noble-gas atoms with halogen-containing compounds *J. Chem. Phys.* **82** 3169–78

[65] Velazco J E, Kolts J H and Setser D W 1978 Rate constants and quenching mechanisms for the metastable states of argon, krypton, and xenon *J. Chem. Phys.* **69** 4357–73

[66] Vallade J and Massines F 2013 Fourier-transformed infrared absorption spectroscopy: A tool to characterize the chemical composition of Ar-NH3-SiH4 dielectric barrier discharge *J. Phys. D. Appl. Phys.* **46** 464007

[67] Bazinette R, Lelièvre J F, Gaudy L and Massines F 2016 Influence of the Discharge Mode on the Optical and Passivation Properties of SiNx:H Deposited by PECVD at Atmospheric Pressure *Energy Procedia* **92** 309–16

[68] Enache I, Caquineau H, Gherardi N, Paulmier T, Maechler L and Massines F 2007 Transport phenomena in an atmospheric-pressure townsend discharge fed by N2/N2O/HMDSO mixtures *Plasma Process. Polym.* **4** 806–14

[69] Wieme W and Lenaerts J 1981 Excimer formation in argon, krypton, and xenon discharge afterglows between 200 and 400 K *J. Chem. Phys.* **74** 483–93

[70] Tschiersch R, Nemschokmichal S and Meichsner J 2017 Influence of released surface electrons on the pre-ionization of helium barrier discharges: Laser photodesorption experiment and 1D fluid simulation *Plasma Sources Sci. Technol.* **26**

[71] Tschiersch R, Bogaczyk M and Wagner H E 2014 Systematic investigation of the barrier discharge operation in helium, nitrogen, and mixtures: Discharge development, formation and decay of surface charges *J. Phys. D. Appl. Phys.* **47**

[72] Li M, Li C, Zhan H, Xu J and Wang X 2008 Effect of surface charge trapping on dielectric barrier discharge *Appl. Phys. Lett.* **92**

[73] Guaitella O, Marinov I and Rousseau A 2011 Role of charge photodesorption in self-synchronized breakdown of surface streamers in air at atmospheric pressure *Appl. Phys. Lett.* **98**

[74] T. H 1947 Imprisonment of Resonance Radiation in Gases T. *Phys. Rev.* **72** 1212

[75] Holstein T 1951 Imprisonment of Resonance Radiation in Gases. II *Phys. Rev.* **83** 1159

[76] Walsh P J 1959 Effect of Simultaneous Doppler and Collision Broadening and of Hyperfine Structure on the Imprisonment of Resonance Radiation *Phys. Rev.* **116** 511–5

[77] Ellis E and Twiddy N D 1969 Time-resolved optical absorption measurements of excited-atom concentrations in the argon afterglow *J. Phys. B At. Mol. Phys.* **2** 1366–77

[78] Wan-Li S, De-Zhen W and Kong M G 2007 Simulation of radio-frequency atmospheric pressure glow discharge in γ mode *Chinese Phys.* **16** 485–92

[79] Moon S Y, Rhee J K, Kim D B and Choe W 2006 α, γ, and normal, abnormal glow discharge modes in radio-frequency capacitively coupled discharges at atmospheric pressure *Phys. Plasmas* **13** 1–7